Drag on superhydrophobic sharkskin inspired surface in a closed channel turbulent flow

K. M. Tanvir Ahmmed, Julian Montagut, and Anne-Marie Kietzig[*]

McGill University, 3610 University Street, Montréal, Québec, H3A 0C5, Canada

ABSTRACT. Salvinia leaf and sharkskin are prime examples of nature's marvel. Salvinia leaf-inspired superhydrophobic surfaces keep themselves clean and reduce drag in fluid flow. Sharkskin also reduces drag in turbulent flow and inhibits biofouling. Therefore, the prospect of having a drag-reducing surface with both salvinia leaf and sharkskin properties is attractive. However, fabricating such a surface is difficult, and the current fabrication methods require at least two separate steps. In addition, the mechanisms of drag reduction of salvinia leaf and sharkskin are different, and their combined effect on the flow field is not well understood. In this study, we produced a PTFE surface that mimics sharkskin in its surface pattern and copies the superhydrophobic nature of the salvinia leaf in its microstructure. This surface was fabricated by laser machining and tested in a closed channel under turbulent flow condition. We measured the pressure drop at different Reynolds numbers on this surface both in pre-wet and non-pre-wet conditions and compared the result with pressure drop data on four other PTFE samples: two types of non-superhydrophobic sharkskin inspired surface (riblets), a superhydrophobic surface, and a non-machined surface. Both the non-superhydrophobic riblets and the superhydrophobic sample reduced drag compared to the non-machined surface. However, we observed a lack of drag reduction by the superhydrophobic riblets sample. We presented a qualitative explanation for the lack of drag reduction and concluded that the modifications of the flow field by the two drag reduction mechanisms are not beneficial for overall drag reduction in our experiment.

KEYWORDS

Superhydrophobic surface, sharkskin, turbulent flow, drag reduction, laser-textured surface.

INTRODUCTION

Drag is the resistance of fluid caused by its motion past a body or a body's motion through it. Energy is needed to overcome drag in all fluid flow applications. Thus, even a small amount of reduction in drag benefits both the environment and the economy. For example, reducing drag in pipelines, which is a case of closed channel flow, can save energy as well as pumping cost. Among different types of drag, form drag and skin friction drag are the most important. Form drag is the

[*] Corresponding author: Tel: +1(514) 398-3302. E-mail: anne.kietzig@mcgill.ca

drag that originates from the shape of the body, whereas skin friction drag is related to the friction between a body and the fluid as well as the friction between adjacent fluid molecules. Reducing skin friction drag is the subject of this study. Both active techniques, such as injecting bubbles, and passive techniques, such as surface modification, are used to reduce skin friction drag [1]. However, passive techniques are preferred over active techniques as no additional energy is required. Nature provided us with two excellent examples of friction drag-reducing surfaces that utilize passive techniques: air-retaining water fern salvinia [2] and dermal denticle covered sharkskin [3].

The salvinia leaf is covered with hairy structures as shown in Figure 1. These hairy structures are essentially dual-scale in nature because of the hydrophobic wax crystals that cover the hairs. The dual-scale roughness of the salvinia leaf renders the surface extremely water-repellent or superhydrophobic (SH). A surface is termed as SH when a water droplet sitting on such a surface makes a contact angle (CA) of larger than 150°, has a contact angle hysteresis of smaller than 10°, which is attributed to trapped air pockets underneath the droplet [4]. Both surface chemistry and roughness features are responsible for superhydrophobicity. Inspired by nature's SH surfaces, such as the salvinia leaf and the lotus leaf, researchers have fabricated artificial SH surfaces that can reduce drag [5-8].

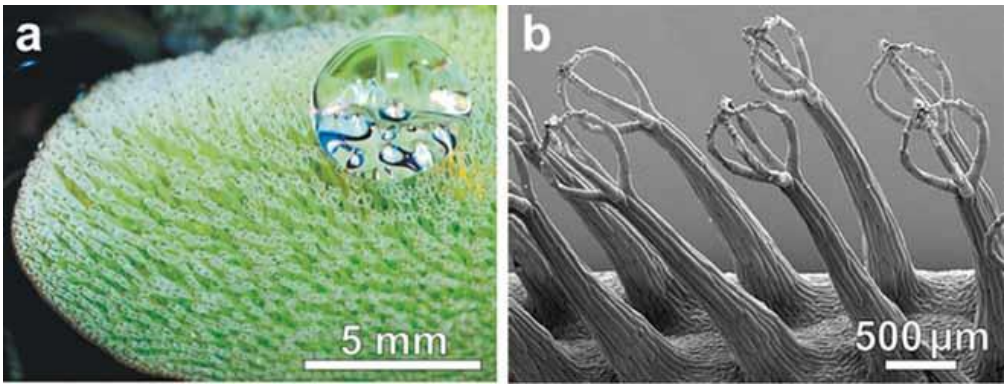

Figure 1. (a) A water droplet sitting on hairy features of a salvinia leaf (b) high resolution image of the hairy features (reprinted from Advanced Materials, Vol 22, Barthlott, W. et al. The Salvinia Paradox: Superhydrophobic Surfaces with Hydrophilic Pins for Air Retention Under Water, p2325, Copyright (2010), with permission from John Wiley and Sons [9]).

Bioinspired SH surfaces reduce drag both in laminar and turbulent flow [10; 11]. The drag reduction mechanism of such a surface in laminar flow is easy to understand. On a SH surface, a

water droplet sits on roughness peaks and is supported by air cushions in the roughness valleys. The drag reduction occurs because of the reduction of solid/water contact area and the creation of a shear-free air/water interface. Accordingly, the no-slip boundary condition at the wall is replaced with an effective slip velocity on a SH surface. The amount of drag reduction by a SH surface can be represented by a parameter called slip length, which is defined as the wall-normal length inside the wall where the velocity would be zero. The larger the slip length, the higher the drag reduction. However, depending on the surface topography, slip can be directional. Slip in the flow direction (streamwise slip) is beneficial, whereas a slip in the spanwise direction is detrimental [12]. While, the picture that we just depicted here is perfect in explaining the drag reduction of a SH surface in laminar flow, experimental and theoretical analysis have shown that the modification of turbulence structures near the wall also affect drag reduction in turbulent flow on a SH surface [6; 13]. Thus, the drag reduction mechanism of a SH surface in turbulent flow is complex, as both the reduction of the solid/water contact area and the modification of turbulences by the surface contribute to drag reduction.

Drag reduction on a SH surface can be increased by reducing the solid/water contact area [14]. This contact area reduction can be achieved by reducing the size of surface features or increasing the distance between adjacent features. However, the spacing between the surface features cannot increase indefinitely; otherwise, the air/water interface will collapse, and the surface will lose its superhydrophobicity. The shape and size of surface features, as well as their arrangements, also have an effect on drag reduction. Different surface features have been used by researchers in drag reduction studies such as ridge structures arranged in the longitudinal and transverse directions to fluid flow, pillar structures arranged in a square lattice, and surfaces with random roughness similar to the salvinia or lotus leaf [15-17].

Another example of nature's drag-reducing surface is given by sharkskin. Sharks are one of the fastest swimmers in nature due to the particular dermal denticles on their skin which reduce skin friction drag compared to a flat surface [18]. The dermal denticles are teeth-like fish scales as pictured in Figure 2(a). Based on their surface chemistry, shark scales are hydrophobic [19]. Structurally, these scales are parallel 3D ridges arranged in an interlocking pattern. However, the geometry and arrangement of these scales vary widely depending on the species [20]. Moreover, scales of the same species differ in shape, size, and geometry depending on their location on the shark's body. Furthermore, the complex 3D nature of sharkskin scales makes it difficult to

replicate and only few fabrication techniques such as bio-replication can mimic the natural sharkskin [21]. However, fabricating such surfaces on different materials on a large scale is challenging. Therefore, most researchers fabricated sharkskin inspired artificial surfaces called riblets that only consider the main aspect of sharkskin: the parallel ridge structures. These riblet surfaces have been shown to be as effective as natural sharkskin in reducing drag [22]. Different fabrication processes such as milling, moulding, and laser etching have been used to fabricate riblets [23].

Much research has been carried out to reveal the mechanism of drag reduction with riblet structures [18; 23]. However, the drag reduction mechanism is still not completely understood [24]. Both natural sharkskins and riblets are only effective in reducing drag in turbulent flow. Dean and Bhushan reviewed and presented the mechanism of drag reduction by riblets in turbulent flow [23]. Turbulent flow is characterized by a laminar-like fluid motion in the viscous sublayer close to the surface and a chaotic fluid motion away from the surface. The viscous sublayer is dominated by streamwise vortices. These vortices move along the flow as well as translate into the cross-flow direction. The interaction between the wall and the vortices as well as the interaction between the adjacent vortices create an outward movement, where the vortices are ejected from the viscous sublayer. All these interactions lead to an increase in the cross-flow velocity vector and contribute to the overall drag. It is believed that the riblet tips lift and pin vortices in the viscous sublayer of turbulent flow. Thus, the translation of streamwise vortices is reduced, which in turn reduces the interaction between adjacent vortices in cross-flow as well as with the wall. Reduced interactions of vortices in the presence of riblets result in reduced outbursts of the vortices from the viscous sublayer. This mechanism of reduced momentum transfer lowers the wall shear stress and therefore reduces skin friction drag [23].

Over the years, researchers have investigated the effect of riblet dimensions and arrangements on drag reduction [25]. Researchers investigated different shapes of riblets such as blade-like, sawtoothed, and scalloped shapes arranged in continuous, aligned segmented, and staggered segmented configurations. The spacing between the adjacent riblets determines whether the streamwise vortices will stay on the riblet tips or enter into the riblet cavities. Thus, the spacing between the riblets (s) is the most important parameter to consider when aiming to optimize riblet design for maximum drag reduction. The height (h), tip size (t), the width of the cavity (w), as shown in Figure 2(b) for a segmented blade riblet, are the other relevant parameters.

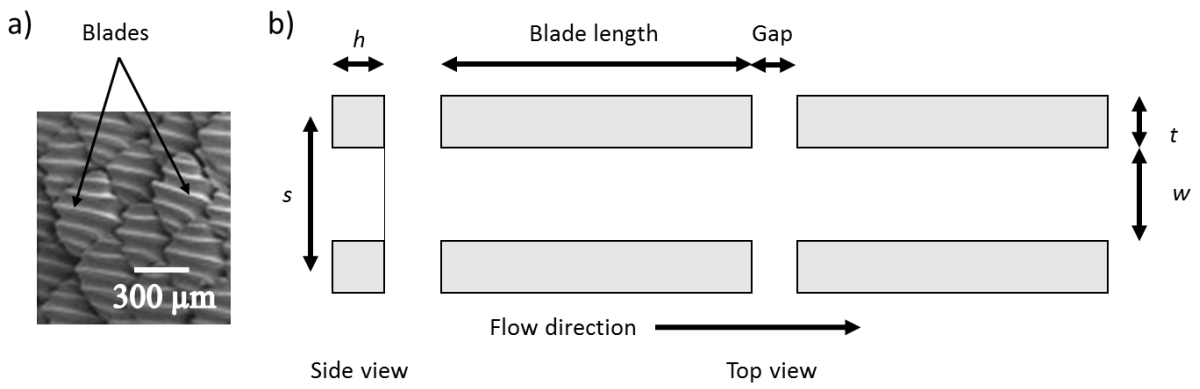

Figure 2. (a) Sharkskin (reprinted from Journal of Colloid and Interface Science, Vol 388, Liu, Y. H. and Li, G. J., A new method for producing "Lotus effect" on a biomimetic sharkskin, p237, Copyright (2012), with permission from Elsevier [26]). (b) Different parameters of a segmented blade riblet aligned with the fluid flow.

Lifting and pinning of vortices at riblet tips are necessary for drag reduction on sharkskin. Thus, the size of the vortices needs to be considered when designing an optimum drag reducing riblet structure. However, as the flow condition changes, so do the dimensions of the vortices. Accordingly, using dimensionless numbers instead of absolute values for the design parameters facilitates the comparison of the results between different flow conditions [23]. The dimensionless spacing (s^+) is defined as

$$s^+ = \frac{sV_\tau}{\nu} \qquad (1)$$

where s is riblet lateral spacing, ν is the kinematic viscosity of the fluid, and V_τ is the wall shear stress velocity which is defined by

$$V_\tau = \left(\frac{\tau_0}{\rho}\right)^{\frac{1}{2}} \qquad (2)$$

where ρ is the fluid density and τ_0 is the wall shear stress that can be calculated from the following equation [25]

$$\tau_0 = 0.03955\nu^{\frac{1}{4}}\rho V^{\frac{7}{4}}D^{-\frac{1}{4}} \qquad (3)$$

where V is the mean flow velocity, and D is the hydraulic diameter of the closed channel. This equation provides an approximate wall shear stress in a smooth closed channel. It is derived by combining the fanning friction factor and Blasius' formula for the friction factor in turbulent flow.

In the case of a rectangular flow cell, as used in our experiment, where *a* is the width of the channel and *b* is the height of the channel, the hydraulic diameter can be calculated by

$$D = \frac{4A}{P} = \frac{2ab}{(a+b)} \qquad (4)$$

where *A* and *P* are the flow area and the wetted perimeter of the flow cell, respectively. Similar to the dimensionless spacing; height and thickness are also calculated in terms of wall units:

$$h^+ = \frac{hV_\tau}{\nu} \qquad (5)$$

$$t^+ = \frac{tV_\tau}{\nu} \qquad (6)$$

The above discussed designing parameters are the only parameters to consider for maximum drag reduction in open channel flow. However, drag reduction by riblets in a closed channel flow differs from the one in open channel flow due to vortices being trapped by the channel walls. Moreover, in closed channel flow, the boundary layer is enclosed by the channel walls, unlike in the open channel flow where the boundary layer grows until it reaches the free stream velocity. Thus, in addition to the riblet dimensions and arrangement, the channel geometry, such as the height of a rectangular channel, affects the performance of riblets in closed channel flow as reported by other researchers [27].

When the two different drag-reducing bioinspired surfaces are compared, it is obvious that the drag reduction mechanism of a SH surface is different from that of a shark riblet as the skin of a shark is not SH. Moreover, the drag reduction mechanism of sharkskin relies only on the geometry of surface features, whereas both surface chemistry and roughness are responsible for superhydrophobicity. Though a SH surface with ridge structures resembles a sharkskin inspired riblet, their respective dimensions are considerably different [12]. The spacing between ridges required for a sharkskin-inspired riblet will lead to an absence of air pockets in surface features. However, the presence of air pockets is necessary for a SH surface. Thus, the only way to fabricate a SH riblet is to fabricate a riblet surface first and then decorate the surface with dual-scale roughness. To the best of our knowledge, two groups, Liu and Li as well as Bixler and Bhushan, have fabricated SH riblets [26; 28]. However, in both cases, two separate fabrication techniques, laser etching combined with coating and molding combined with flame treatment, were necessary for the surface fabrication. Only Bixler and Bhushan studied the drag reduction on such a surface and

reported an improvement in drag reduction compared to a non-SH riblet [28]. However, the combined effect of two different drag reduction mechanisms on the flow field was not studied.

In this work, we developed a novel method for fabricating SH riblets by using a single fabrication technique: laser micromachining. We compared the drag on the SH riblets with a SH surface and two non-SH riblets both in pre-wet condition and non-pre-wet condition. Moreover, the effect of two different drag reduction mechanisms on the flow field was investigated by analyzing the observed drag reduction behaviors.

MATERIALS AND METHODS

Sample Design

We studied the drag on continuous blade type riblets, whose dimensionless parameters we based on the best available optimized data found in Dean and Bhushan's as well as Bixler and Bhushan's works [23; 27]. For a closed channel turbulent flow, $s^+ \approx 15$ was found to be the optimized spacing for drag reduction, whereas the height and thickness needed to be small. Guided by these design considerations we designed two types of riblet surfaces (type I and type II) by keeping the s^+ value constant at 15 and varying the height of the blades. Based on our initial drag reduction results, we choose the tall blade riblets for fabricating the SH shark riblets. The samples used in this study are listed in Table 1 along with their associated parameters.

Table 1. Sample types and related parameters.

Sample name	**Surface topography (blade parameters)**						
	Spacing (μm)	**Height (μm)**	**Thickness (μm)**	**Width (μm)**	**s^+**	**h^+**	**t^+**
Type I riblet	173	73	45	128	15	6.3	3.9
Type II riblet	173	37	45	128	15	3.2	3.9
SH riblet	173	73	45	128	15	6.3	3.9
	Surface topography						
SH	Dual-scale micro/nano roughness						
Flat PTFE	Microscopically smooth						

Sample Fabrication by Laser Micromachining

A femtosecond laser system (amplified Ti:Sapphire, Coherent Libra) was used to fabricate the samples. The laser system has a wavelength of 800 nm, and repetition rate of 1 kHz. Polytetrafluoroethylene (PTFE) sheets were used as the samples and were purchased from McMaster-Carr. A horizontally-polarized Gaussian beam of ~5 mm ($1/e^2$ beam diameter) was focused on the samples with a 100 mm plano-convex lens. The samples were positioned on a computer-controlled 3D translation stage (Newport Corporation) at the focal plane of the laser beam. The scanning scheme for material ablation was controlled by this stage in conjunction with a shutter. GOL3D software (GBC&S) was used to program both the stage and the shutter. The power of the laser beam was varied by a computer-controlled variable attenuator which consists of a half-wave plate and a polarizing beam splitter.

The beam diameter at the focal plane (~20 μm) is smaller than the designed riblet width (128 μm) in our setup. Thus, a raster scanning method was employed to fabricate the desired width. Raster scanning was also used to fabricate the SH surface. The line overlap was calculated from the single scan experimental line width and the movement of the stage in a direction perpendicular to the scanning direction. The power of the laser beam was varied between 40 mW and 100 mW, whereas the line overlap was varied between 70% and 80% for fabricating different types of surfaces. The pulse durations were ~10 ps for the riblet samples and ~100 fs for the SH sample. The laser micromachining process was carried out in air. After laser micromachining, the samples were cleaned in an ultrasonic acetone bath for five minutes.

Surface Analysis

Scanning electron microscopy (SEM) (FEI Inspect F50) was used to image the cross-sectional view of the ablated lines. A 10 nm thick gold coating was applied by an SPI-Module sputter coater before the imaging. Other images were taken by an FEI Quanta 450 FE-SEM in low vacuum mode. No coating was necessary for the latter instrument. A Leica EZ4 D optical microscope was used to determine the single-scan line widths.

Advancing and receding CAs were measured with a goniometer (Data Physics OCA 15EC) at room temperature with reverse osmosis (RO) water as the test fluid. An initial droplet size of 5 μL was used in the measurements. The droplet size was increased to 8 μL with a dispense rate of 0.1 μL/s for measuring the advancing contact angle, whereas the droplet was reduced from 8 μL to the initial size for receding contact angle measurements. The reported values of contact angles are an average of three replicates.

Pressure Drop Measurement

Pressure drop measurements were carried out in a horizontal rectangular flow cell. The top side of the flow cell holds the sample surface. The channel was then sealed so that it is leak proof. The dimension of the channel is 300 mm × 10 mm × 2 mm. A differential pressure gauge (DPG 409-10WDWU, Omega) connected to the bottom wall of the flow cell was used for pressure drop measurements. The distance between the two ports of the gauge is 30 mm, and the first port is located 220 mm away from the entrance of the flow cell. Therefore, no entrance effect is expected in the experiments. A source tank filled with RO water was connected to a high-pressure N_2 gas cylinder. The flow rate was controlled by regulating the gas pressure and by a valve installed in the flow line. A needle valve was also used to fine tune the flow rate. A turbine flow meter (FTB 504, Omega) was used to measure the flowrate. A schematic diagram of our setup is shown in Figure 3.

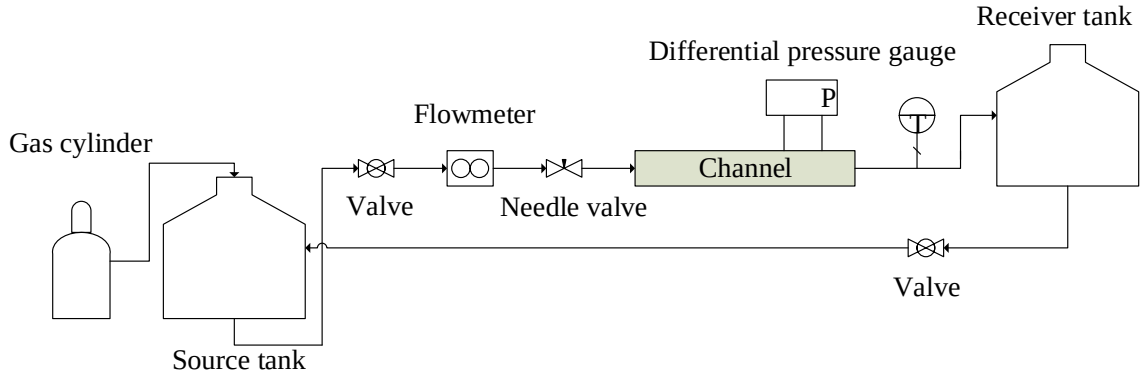

Figure 3. Schematic diagram of the flow cell setup used to measure the pressure drop on different surfaces (Reprinted with permission from K. M. T. Ahmmed, C. Patience, and A.-M. Kietzig, ACS Applied Materials & Interfaces, 2016, 8, 27411-27419. Copyright (2016) American Chemical Society [29]).

Flow rates were varied between 1500 and 2000 mL/min to achieve turbulent flow. The water temperature was measured with a thermocouple attached to a digital readout. Flat PTFE samples were used as the control surfaces for pressure drop measurements. Some of these control samples were later used for fabricating the sharkskin samples. The pressure drop results are shown in Figure S1 of the supplementary information. We conducted two sets of experiments for all the samples to decouple the two drag reduction mechanisms from each other by running the experiments with pre-wetted and non-pre-wetted samples. The motivation behind using pre-wetted samples is that all the pre-wetted samples will act as superhydrophilic samples irrespective of their previous

wetting state. For experiments with pre-wetted samples, the samples were first dipped in an ethanol solution. Then, the surface was rinsed with RO water and directly used in the flow cell experiments.

RESULTS AND DISCUSSION

Surface Structures and Wetting

Figure 4 shows a SH sample surface which does not have any ridge structure. Figure 4 (b and c) show that the SH surface is covered with hierarchical micro/nano structures. The roughness of the laser-ablated SH surface is about an order of magnitude higher than that of a flat non-ablated surface. The arithmetic average roughness, R_a was measured as 0.025 and 0.262 µm for a flat PTFE and the SH sample, respectively [29]. The roughness measurements presented here are an approximation and obtained by 3D confocal microscopy.

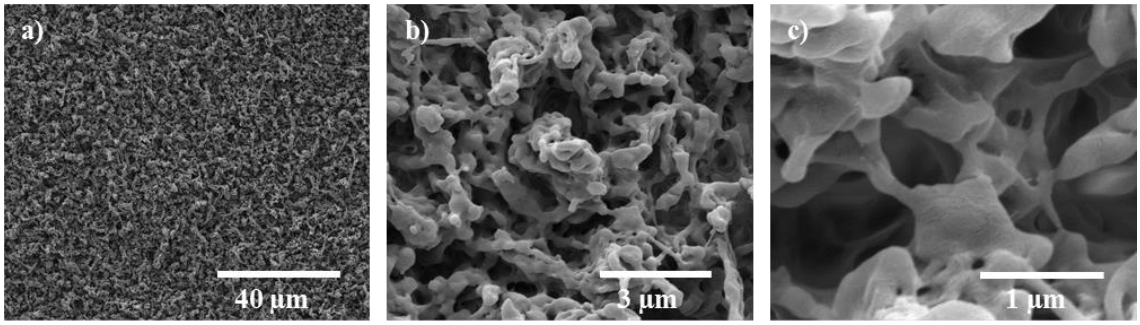

Figure 4. Scanning electron micrographs (SEM) of the SH sample at different magnifications (adapted with permission from K. M. T. Ahmmed, C. Patience, and A.-M. Kietzig, ACS Applied Materials & Interfaces, 2016, 8, 27411-27419. Copyright (2016) American Chemical Society [29]).

Figure 5 shows the SEM images of the riblet samples. Laser-machined lines are overlapped to fabricate a single trench (Figure 5 a and b). The ablated trenches are nearly rectangular and resemble the blade type of riblets. The trenches were arranged in such a way that they simulated the segmental streamwise blade configuration. The type I riblet (Figure 5a) is deeper than the type II riblet (Figure 5b). Figure 5c illustrates the top view of the type I riblet sample. It is to note that the top view of the type II riblet sample looks alike as presented in Figure S2 of the supplementary information. Accordingly, for the type I and II riblet samples (Figure 5c and Figure S2), only the bottom and side walls of the trenches are decorated with hierarchical micro/nano structures that are characteristic of PTFE laser ablation. The top surfaces (tips of the blades) constitute the original

flat PTFE sample. In contrast, the SH riblet sample (Figure 5d) is entirely covered with hierarchical structures.

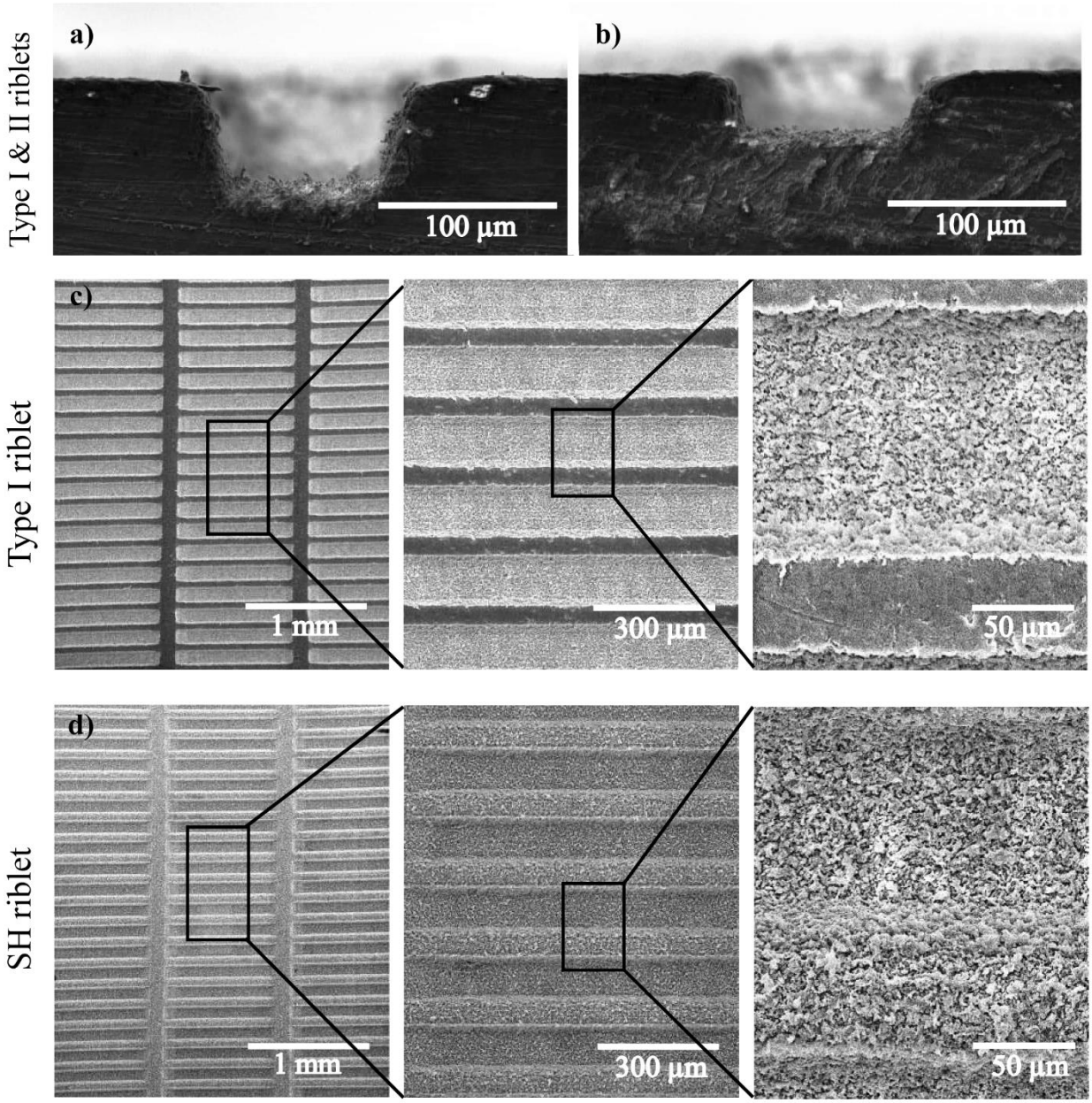

Figure 5. Vertical cross-sectional view of the laser ablated trenches for fabricating (a) type I and (b) type II riblet samples. Top view of (c) the type I riblet and (d) SH riblet samples at different magnifications.

Wetting characteristics of all the samples are shown in Figure 6, and the respective contact angles are listed in Table 2. Contact angles (CA) measured on the riblet structures depend on the orientation of the sample as the riblet samples are not isotropic. Thus, we measured the contact

angles both in the longitudinal and transverse directions of the pattern. Though the side walls and bottom of the type I and type II riblet samples were hierarchical in nature, these surfaces were not superhydrophobic as the tips of the riblets are flat and not covered with hierarchical structures.

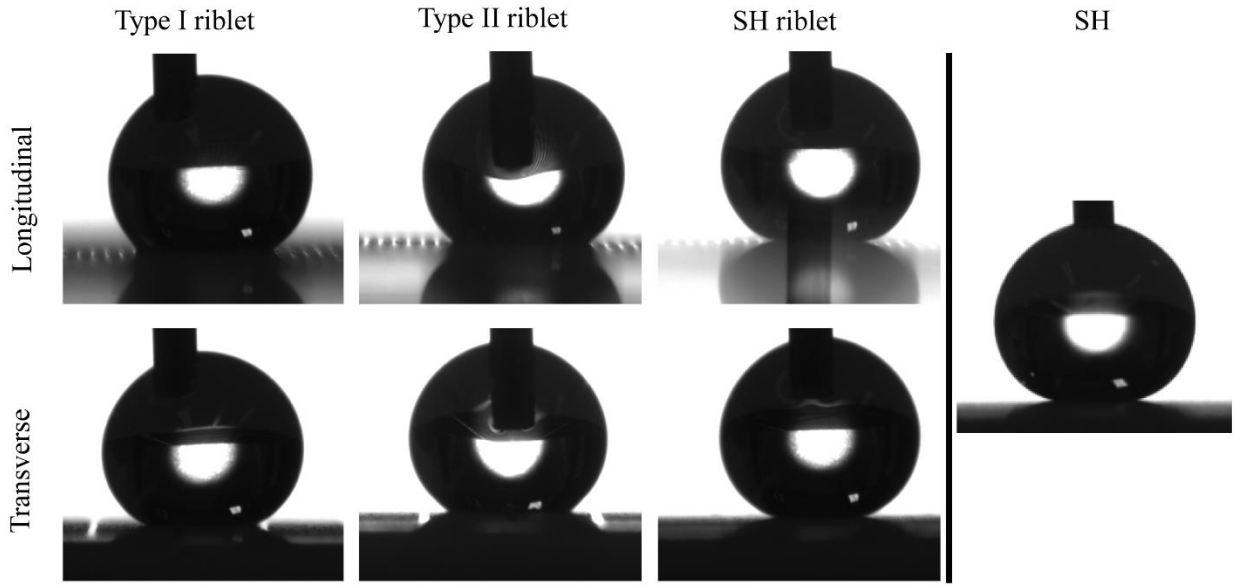

Figure 6. Water droplets (8 µL) sitting on the samples.

In contrast to the riblet samples, the SH sample showed an advancing contact angle of 160 ± 1° and a contact angle hysteresis of 2 ± 1°. The SH riblet sample showed similar wetting behavior as the SH surface. Trapped air pockets under the water droplet sitting on the SH surface were verified by using a confocal microscope in our earlier study [29]. Moreover, both the SH and SH shark surfaces sustained the air-trapping wetting state (also called the Cassie state) during flow experiments as verified by visual inspection and shown in Figure S3 in the supplementary information. No wetting occurred on the ablated SH surfaces. In contrast, both the riblet samples were visibly wet after the tests.

Table 2. Wetting characteristics of the surfaces.

Sample	Advancing CA, °		Receding CA, °	
	Longitudinal	**Transverse**	**Longitudinal**	**Transverse**
Type I riblet	124 ± 1°	141 ± 2°	119 ± 1°	132 ± 4°
Type II riblet	128 ± 6°	140 ± 4°	123 ± 6°	133 ± 4°
SH riblet	157 ± 1°	151 ± 4°	153 ± 2°	147 ± 4°
SH	160 ± 1°		158 ± 1°	
Flat PTFE	107± 2° (sessile CA) [30]			

Pressure Drop

Pressure drop was measured on all the samples both in pre-wetted and non-pre-wetted conditions and plotted against the Reynolds number as shown in Figure 7. In all the plots, the dashed line represents the regression line for the pressure drop data on a flat PTFE sample. The regression lines for the pressure drop data of all other samples are presented with dotted lines. We noticed a measurable reduction in pressure drop both for type I (Figure 7(a)) and type II (Figure 7(b)) riblet samples when compared to the pressure drop measurements on the flat PTFE sample. The slopes of the two regression lines (one for the flat PTFE sample, another for the pre-wetted type I riblet sample and the type II riblet sample) are significantly different (P=0.034 and 0.003, respectively). Thus, we conclude that both the shark samples are able to reduce drag in turbulent flow. Though it was expected that the shark samples would reduce drag, the amount of drag reduction is lower than anticipated. The maximum drag reduction we observed is only 4%. A drag reduction of ~20% was reported by Bixler and Bhushan on riblet samples with design parameters similar to the current study in a closed channel with the turbulent flow of water [25].

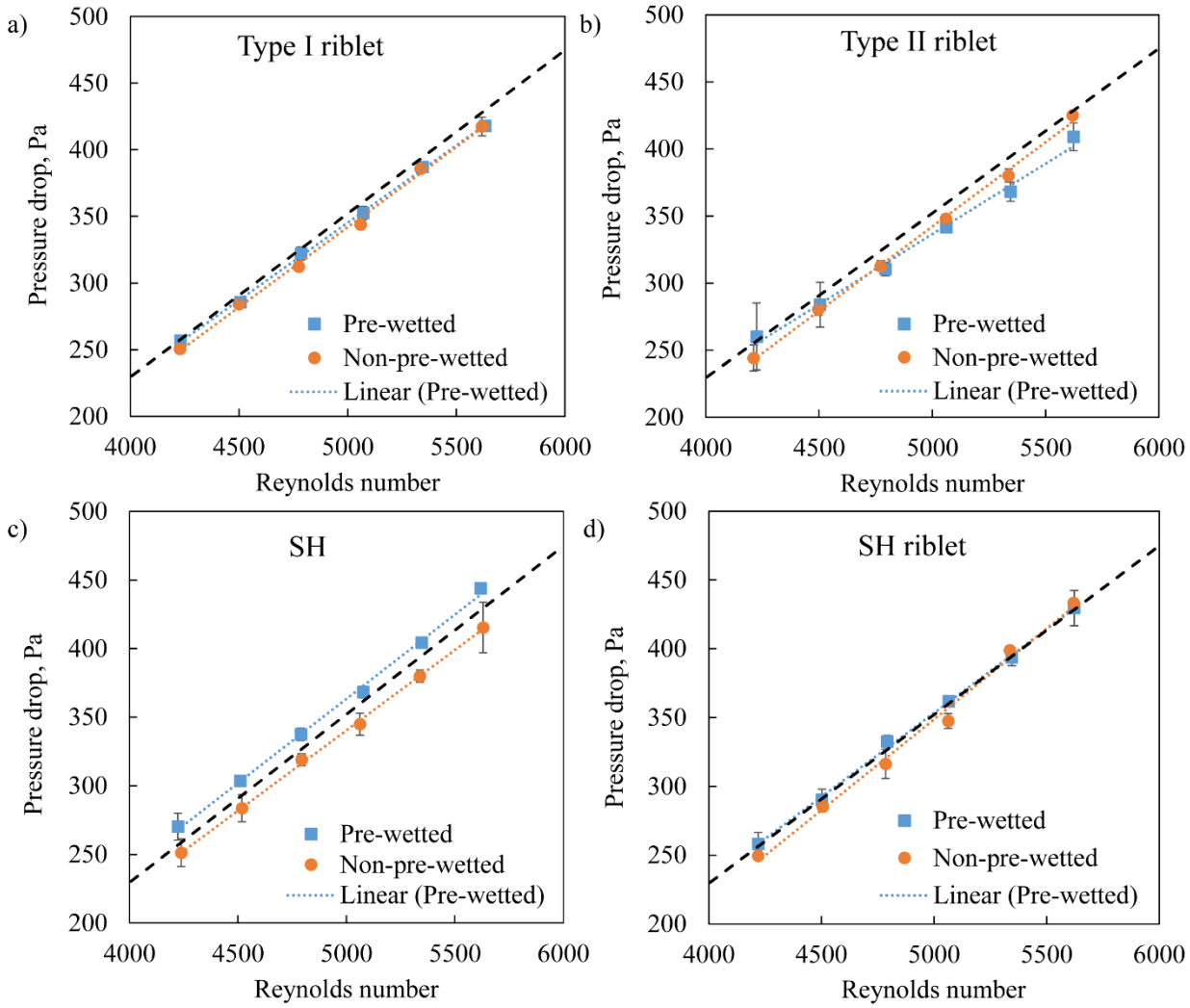

Figure 7. Change in pressure drop with increasing Reynolds number for (a) type I riblet, (b) type II riblet, (c) SH, and (d) SH riblet samples. Both pre-wetted and non-pre-wetted data are plotted for each sample. The dashed and dotted lines represent the best-fitted lines for measured pressure drops. The error bars in the figure represent the standard deviation for three replicates.

Next, we compared the drag reduction from the two types of riblet samples (Figure 7(a and b)). The slopes of the two regression lines of the pre-wetted samples are not significantly different (P=0.113). Therefore, we conclude that the effect of a change in riblet height is not obvious from our experimental results. Moreover, we found no differences in pressure drop between pre-wetted and non-pre-wetted conditions as the slopes of the respective regression lines are not significantly different (P=0.102) as shown in Figure 7(a).

Similar to the experiments conducted with the riblet samples, we measured the pressure drop on the SH sample and SH riblet sample. We only used the design parameters of the type I riblet sample

to fabricate the SH riblets because we did not find any differences in drag reduction between the two types of riblets. The SH surface (Figure 7(c)) reduced drag in its non-pre-wetted condition. The amount of drag reduction is small because the slip length on this PTFE SH sample is small (~ 13 μm) as observed earlier in a laminar flow experiment [29]. However, when the sample is pre-wetted, the drag reduction disappeared, instead, increase in the pressure drop is observed compared to a flat PTFE sample and the non-pre-wetted SH sample. The intercepts of the two regression lines (one for the pre-wetted SH sample another for the non-pre-wetted SH sample) are significantly different (P<0.0001), which confirms that the pre-wetted SH sample indeed increased drag. The water contact area on a pre-wetted SH sample is higher than that of the non-pre-wetted SH sample. On a non-pre-wetted SH sample, water is in contact with only the tips of the roughness features, whereas on a pre-wetted SH sample water is in contact both with the tips of the roughness features and the valleys. This increased water contact area contributes to the increased pressure drop of the pre-wetted SH sample compared to the non-pre-wetted SH sample.

Unlike the other three samples (type I riblet, type II riblet, and the SH sample), the SH riblet sample did not reduce drag. No synergistic effect of the two different drag reduction mechanisms was observed as seen in Figure 7 (d). Both the pre-wetted and non-pre-wetted samples showed similar behavior. The slopes of the two regression lines (one for the non-pre-wetted another for the pre-wetted SH shark sample) are not significantly different (P=0.08). This lack of drag-reducing behavior of the non-pre-wetted SH sharkskin sample was surprising. Thus, we further looked into the near-wall phenomena. As two different mechanisms are involved, at first we decoupled them to explain the results, then we considered the mechanisms together. For explaining the effect of superhydrophobicity in the riblet structure, we will compare it to a flat SH sample. The water contact area for the riblet sample is 84% larger than the water contact area of a flat SH sample considering the per unit projected area of the sample, which is qualitatively explained in Figure 8.

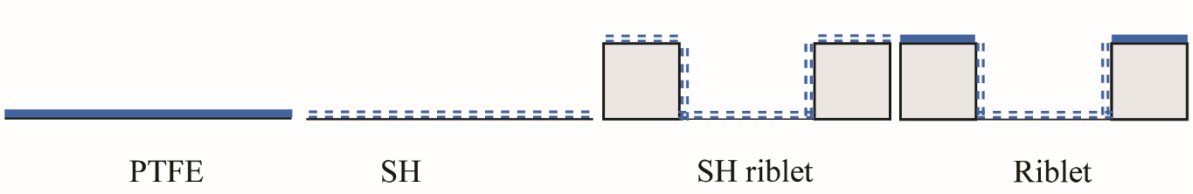

Figure 8. Schematic of a vertical cross section of the PTFE, SH, SH riblet, and riblet samples. The solid blue line represents the water contact with the sample surface, whereas the dashed blue line indicates the water contact with solid and air pockets. The solid blue line represents higher solid/water contact area compared to a dashed line.

The effect of the shear-free area decreased as the water contact area increased in the SH shark sample compared to a SH sample. Therefore, the small drag reduction achieved by the SH mechanism was neutralized or even surpassed by increased drag due to the large water contact area on a SH shark sample. However, this may not be the only reason behind the lack of drag reduction on the SH shark sample. The hierarchical nature of both the SH and SH shark samples rendered them to isotropic slip surfaces. Both longitudinal slip and spanwise slip are present on these surfaces. Clearly, the effect of drag reducing longitudinal slip is higher than the drag-increasing spanwise slip on our SH sample [31]. However, this spanwise slip on the SH shark surface can interfere with the drag reduction mechanism of the riblets. It is well known that the spanwise slip increases the streamwise turbulence intensity [12]. Thus, the pinning and cross-flow of streamwise vortices can be influenced by the spanwise slip. Movement along the flow and cross-flow translation of vortices likely increases drag on the SH shark sample. For the pre-wetted SH shark sample, presented in Figure 7d, the effect of superhydrophobicity is not present, which means that the flow field was not influenced by spanwise slip. Thus, drag reduction originating solely by the riblet drag reduction mechanism could be expected. However, in this scenario, the sample area in contact with water is larger than in any other sample, as water penetrates the micro/nano structures present in both the tips and grooves of riblet structures. Thus our results illustrate that the increased drag caused by the increased wetted area is not overcome by the riblet induced drag reduction.

The explanation provided here can also explain the lower drag reduction, compared to what was observed earlier by Bixler and Bhushan [27], on both type I and type II riblet samples used in our experiments as they have a dual-scale roughness in the riblet valleys. However, the reason behind the lack of difference in drag reduction between type I and type II riblet samples is not clear. We

do note that other parameters such as the height of the flow cell, the position of the sample (top or bottom wall) might have an effect on overall drag reduction as observed by other researchers [27]. However, as the vortices are one order of magnitude smaller than the channel height, the effect of channel height will be marginal in our experiment. Further experiments with no dual-scale roughness in the riblet valleys and side walls for the type I and type II samples could provide drag reduction results for better comparison with the literature values. Unfortunately, this is not possible by using our current method of fabrication. As for the SH shark sample, experiments need to be conducted with surfaces having large slip length to further investigate the combined effect of both drag reduction mechanisms in play.

CONCLUSION

A novel method for fabricating a superhydrophobic (SH) riblet sample is presented in this study. The drag on this surface was compared with two non-SH riblet samples, a SH sample, and a non-machined flat sample. Both the non-SH riblet samples and the SH sample reduced drag compared to the flat sample. However, the amount of drag reduction by the riblets did not correspond well with the literature values although the riblets were designed for maximum drag reduction. In addition, riblet height did not affect drag reduction in our experiments. Surprisingly, the SH shark sample showed no drag reduction. The lack of drag reduction is explained by considering both the SH and shark drag reduction mechanisms. The large water contact area of a SH riblet sample diminished the benefit of drag reduction from the SH drag reduction mechanism. Moreover, spanwise slip on the SH riblet sample can interrupt the riblet drag reduction mechanism. Finally, we concluded that the manipulation of the flow field by two different mechanisms of drag reduction is not always beneficial for obtaining a synergistic effect.

ACKNOWLEDGEMENT

This research was funded by the Natural Sciences and Engineering Research Council of Canada (NSERC) and the Fonds de recherche du Québec–Nature et technologies (FRQNT). The authors acknowledge the help from the members of the surface engineering group at McGill.

AUTHOR INFORMATION

Author Contributions

K. M. Tanvir Ahmmed wrote the manuscript, designed and conducted all the experiments, and all the analyses. Julian Montagut participated in part of the pressure drop experiments and edited the manuscript. Anne-Marie Kietzig supervised the work and edited the manuscript.

Notes

The authors declare no competing financial interest.

REFERENCES

[1] M. Gad-el-Hak, *Appl. Mech. Rev.* **1989**, *42*, 261.

[2] W. Barthlott, M. Mail, C. Neinhuis, *Phil. Trans. R. Soc. A.* **2016**, *374*, 20160191.

[3] M. J. Walsh, *AIAA J.* **1983**, *21*, 485.

[4] E. Bormashenko, *Adv. Colloid Interface Sci.* **2015**, *222*, 92.

[5] Y. C. Jung, B. Bhushan, *J. Phys.-Condes. Matter*. **2010**, *22*, 035104.

[6] J. P. Rothstein, "Slip on Superhydrophobic Surfaces," *Annual Review of Fluid Mechanics*, Annual Reviews, Palo Alto **2010**, p. 89-109.

[7] S. F. Toosi, S. Moradi, M. Ebrahimi, S. G. Hatzikiriakos, *Appl. Surf. Sci.* **2016**, *378*, 426.

[8] S. F. Toosi, S. Moradi, S. Kamal, S. G. Hatzikiriakos, *Appl. Surf. Sci.* **2015**, *349*, 715.

[9] W. Barthlott, T. Schimmel, S. Wiersch, K. Koch, M. Brede, M. Barczewski, S. Walheim, A. Weis, A. Kaltenmaier, A. Leder, H. F. Bohn, *Adv. Mater.* **2010**, *22*, 2325.

[10] J. Ou, B. Perot, J. P. Rothstein, *Phys. Fluids*. **2004**, *16*, 4635.

[11] M. A. Samaha, H. V. Tafreshi, M. Gad-el-Hak, *CR. Mecanique*. **2012**, *340*, 18.

[12] B. Woolford, J. Prince, D. Maynes, B. W. Webb, *Phys. Fluids*. **2009**, *21*, 085106.

[13] N. B. Spencer, L. L. Lee, R. N. Parthasarathy, D. V. Papavassiliou, *Can. J. Chem. Eng.* **2009**, *87*, 38.

[14] T. Lee, E. Charrault, C. Neto, *Adv. Colloid Interface Sci.* **2014**, *210*, 21.

[15] K. M. T. Ahmmed, A. M. Kietzig, *Soft Matter*. **2016**, *12*, 4912.

[16] C. H. Choi, C. J. Kim, *Phys. Rev. Lett.* **2006**, *96*, 066001.

[17] M. Ebrahimi, V. K. Konaganti, S. Moradi, A. K. Doufas, S. G. Hatzikiriakos, *Soft Matter*. **2016**, *12*, 9759.

[18] D. W. Bechert, M. Bruse, W. Hage, *Exp. Fluids*. **2000**, *28*, 403.

[19] D. Zhao, Q. Tian, M. Wang, Y. Jin, *J. Bionic Eng.* **2014**, *11*, 296.

[20] W.-E. Reif, *Squamation and ecology of sharks*, Senckenbergische Naturforschende Gesellschaft, Frankfurt am Main **1985**, p. 101.

[21] H. W. Chen, X. Zhang, L. X. Ma, D. Che, D. Y. Zhang, T. S. Sudarshan, *Appl. Surf. Sci.* **2014**, *316*, 124.

[22] S.-J. Lee, S.-H. Lee, *Exp. Fluids*. **2001**, *30*, 153.

[23] B. Dean, B. Bhushan, *Phil. Trans. R. Soc. A.* **2010**, *368*, 4775.

[24] W. Li, C. W. James, J. M. T. Patrick, V. L. George, *Bioinspir. Biomim.* **2015**, *10*, 066010.

[25] G. D. Bixler, B. Bhushan, *Adv. Funct. Mater.* **2013**, *23*, 4507.

[26] Y. Liu, G. Li, *J. Colloid Interface Sci.* **2012**, *388*, 235.

[27] G. D. Bixler, B. Bhushan, *J. Colloid Interface Sci.* **2013**, *393*, 384.

[28] G. D. Bixler, B. Bhushan, *Soft Matter*. **2012**, *8*, 11271.

[29] K. M. T. Ahmmed, C. Patience, A.-M. Kietzig, *ACS Appl. Mater. Interfaces*. **2016**, *8*, 27411.

[30] F. Liang, J. Lehr, L. Danielczak, R. Leask, A. M. Kietzig, *Int. J. Mol. Sci.* **2014**, *15*, 13681.

[31] A. Busse, N. D. Sandham, *Phys. Fluids*. **2012**, *24*, 055111.

NOMENCLATURE

Symbol	Description	Unit
a	Channel width	m
A	Flow area	m^2
b	Channel height	m
D	Hydraulic Diameter	m
h	Riblet height	m
h^+	Dimensionless height	
P	Wetted perimeter	m
s	Riblet lateral spacing	m
s^+	Dimensionless spacing	
t	Riblet tip width	m
t^+	Dimensionless riblet tip width	
V	Mean flow velocity	m/s
V_τ	Wall shear stress velocity	m/s
w	Riblet cavity width	m
	Greek letters	
ν	Kinematic viscosity	m^2/s
ρ	Density	kg/m^3
τ_0	Wall shear stress	N/m^2